
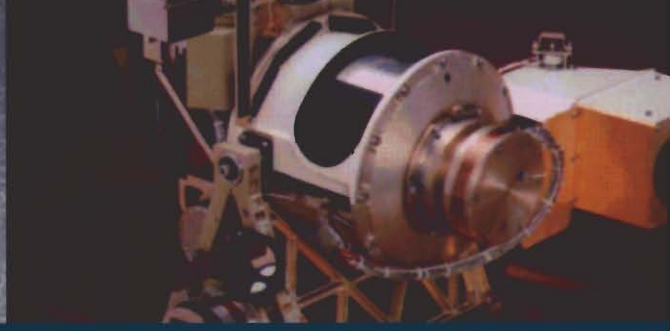

REMOTE SENSING
of the Marine Environment

Manual of Remote Sensing
Third Edition, Volume 6


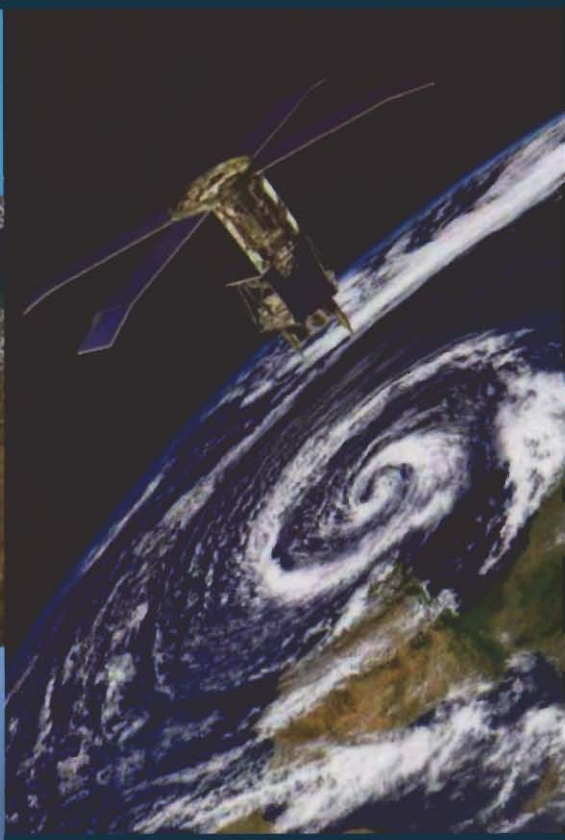


edited by **James F.R. Gower**

Chapter

2

Large-scale Ocean Circulation

Author: Gregg Jacobs

2.1 INTRODUCTION

This chapter examines the observation and physics of large-scale ocean features. Physical oceanographers apply the term "large-scale" to features with characteristic horizontal sizes much greater than the vertical. This requirement is often referred to as the shallow water approximation since the ocean features appear to be horizontally very broad and vertically very thin across the globe. Throughout much of the ocean interiors, away from the coasts and continental shelves, ocean depths range from 2 to 5 km and can extend further in deep ocean trenches. Based on historical ship-derived observations, the horizontal extent of deep ocean circulation features ranges from 20 km to 20,000 km and are thus large scale. Of course, on the continental shelves where depths are on the order of 100 m, horizontal scales may be much smaller to qualify as large scale.

The advantage of restricting examination to large-scale ocean features lies in the simplifications that may be made to the equations governing the evolution of the ocean dynamics. The solution of the three-dimensional Navier-Stokes equations in a rotating coordinate frame is extremely cumbersome. Any reduction in the complexity of the dynamical system is welcome. Such simplifications ease the solution processes that may involve either analytic solution of the equations or numerical representation of the dynamical equations. Simplified equations and their solutions lead to a better understanding of the fundamental physics controlling the oceans.

We begin this chapter by examining the dynamical equations and the simplifications that are allowed through the large-scale assumption. The simplified equations immediately illuminate the importance of the sea surface height (*SSH*), which is the deviation of the ocean surface from its position if the ocean were at rest and no forcing were applied. With this in mind, we then examine how *SSH* measurements may be obtained from satellite altimeter instruments. Several ocean process examinations provide examples to demonstrate the use of altimeter measurements.

2.2 THE IMPORTANCE OF SSH

If the ocean were at rest and no forcing were applied, the ocean surface would lie along a gravitational geopotential surface referred to as the geoid. Consider an area of the ocean over which the water surface is above the geoid. This water mass produces a pressure anomaly

throughout the underlying water column. Horizontal variations in the sea level relative to the geoid produce horizontal pressure gradients, and the horizontal pressure gradient is one of the primary forcing terms in the Navier-Stokes equations that govern the development of the ocean circulation. This derivation is outlined below.

Define a local coordinate system with the x direction positive eastward, y positive northward, and z the distance above the local geoid. The manner through which sea level affects pressure throughout the fluid may be seen in the vertical momentum balance equation, which is (ignoring frictional stresses and Coriolis force in the vertical direction)

$$\frac{\partial \rho w}{\partial t} + \frac{\partial \rho wu}{\partial x} + \frac{\partial \rho wv}{\partial y} + \frac{\partial \rho ww}{\partial z} + \frac{\partial p}{\partial z} - \rho g = 0 \qquad (2\text{-}1)$$

where g is the magnitude of the gravitational acceleration, ρ is the sea water density, p is the pressure, and u, v and w are the three components of the velocity field in the eastward, northward and upward directions. The assumption that the ocean circulation is large scale may be used to examine the magnitude of each of the terms in Equation 2-1. Pedlosky (1987) discusses the details of this analysis. The large-scale assumption leads to the conclusion that the vertical velocity tendency ($\frac{\partial \rho w}{\partial t}$) and advective terms ($\frac{\partial \rho wu}{\partial x} + \frac{\partial\, \rho wv}{\partial y} + \frac{\partial \rho ww}{\partial z}$) are much smaller than the gravitational acceleration or the vertical pressure gradient. Equation 2-1 reduces to the hydrostatic approximation

$$\frac{\partial p}{\partial z} = \rho g \qquad (2\text{-}2)$$

There are significant ocean processes for which Equation 2-2 does not hold. These processes involve large vertical movements of water masses over short horizontal distances, which violate the large-scale assumption. Thus, we must keep in mind that our equations represent a subset of ocean processes. Fortunately, the subset of large-scale processes contains a vast range of very important processes. *In situ* observations have borne out that large-scale ocean features do indeed have dynamics described by the hydrostatic approximation.

One additional assumption aids in further simplifying the dynamical equations without inducing significant errors. The Bousinesque approximation assumes that density variations from the mean are small. Thus, density is given by $\rho = \rho_0 + \rho'(x, y, z, t)$ where ρ_0 is a mean density constant throughout all space and time, and the density perturbations $\rho'(x, y, z, t)$ are much smaller than the mean. In addition, the density perturbations are retained only when multiplied by gravity in the vertical momentum equation. The pressure at any depth is obtained by integrating the hydrostatic approximation (Equation 2-2) from the depth of interest to the sea surface, with the constant of integration determined by the requirement that pressure at the sea surface (at $z=h(x,y)$) be equal to the atmospheric pressure $A(x,y,t)$

$$p = \int_z^{h(x,y)} \left(\rho_o + \rho'(x,y,z',t)\right) g dz' = g\rho_o \left(h(x,y) - z\right) + \int_z^{h(x,y)} \rho'(x,y,z',t)\, g dz' + A(x,y,t) \quad (2\text{-}3)$$

Within the horizontal momentum equations, the pressure gradient forces velocity changes. By the Bousinesque assumption, density variations are not significant, and thus density is specified as the constant ρ_0

$$\frac{\partial u}{\partial t} + \frac{\partial}{\partial x}(uu - \frac{1}{\rho_o}\tau_{xx}) + \frac{\partial}{\partial y}(uv - \frac{1}{\rho_o}\tau_{yx}) + \frac{\partial}{\partial z}(uw - \frac{1}{\rho_o}\tau_{zx}) - fv + \frac{1}{\rho_o}\frac{\partial p}{\partial x} = 0 \quad (2\text{-}4)$$

$$\frac{\partial v}{\partial t} + \frac{\partial}{\partial x}(uv - \frac{1}{\rho_o}\tau_{xy}) + \frac{\partial}{\partial y}(vv - \frac{1}{\rho_o}\tau_{yy}) + \frac{\partial}{\partial z}(vw - \frac{1}{\rho_o}\tau_{zy}) + fu + \frac{1}{\rho_o}\frac{\partial p}{\partial y} = 0 \quad (2\text{-}5)$$

where f is the Coriolis parameter and frictional stresses are provided in flux form by τ_{ij}.

Assume the ocean density were constant ($\rho' = 0$). This is one class of fluid flows referred to as barotropic. Also assume atmospheric pressure does not vary spatially. Then the hydrostatic approximation (Equation 2-3) may be used to provide the horizontal pressure gradients

$$\frac{1}{\rho_o}\frac{\partial p}{\partial x} = g\frac{\partial h}{\partial x} \quad (2\text{-}6)$$

$$\frac{1}{\rho_o}\frac{\partial p}{\partial y} = g\frac{\partial h}{\partial y} \quad (2\text{-}7)$$

Thus sea level measurements provide one of the most important forcing terms in the equations governing the ocean circulation and its temporal development. Sea level deviations from the ocean rest state produce pressure on the water below, and horizontal sea level variations imply horizontal pressure gradient forces that change the circulation.

The derivation outlined above includes many assumptions. Some of the largest real-world deviations from this simple interpretation of sea level in the ocean occur due to density variations (violating the assumption that $\rho'(x, y, z, t) = 0$). In many areas, temperature and salinity variations throughout the ocean produce density changes sufficient to force first-order changes in the ocean circulation. Thus, while not the entire picture, the sea surface height is certainly a major contributor.

A further analytic relation between the flow field and the *SSH* may be obtained from the momentum, Equations 2-4 and 2-5, and the horizontal pressure gradients, Equations 2-6 and 2-7. Assume frictional forces and nonlinear tendencies are small and that the fluid is in steady state. The result is the geostrophic balance

$$u = -\frac{g}{f}\frac{\partial h}{\partial y} \tag{2-8}$$

$$v = \frac{g}{f}\frac{\partial h}{\partial x} \tag{2-9}$$

This provides a direct connection between the *SSH* and the velocity under the restrictions outlined above. Measurements in the deep ocean have provided evidence that the hydrostatic balance is satisfied relatively well. Thus, the primary forces balancing the ocean circulation at the large scale are the horizontal pressure gradient and the Coriolis force. Satellite altimeter instruments provide measurements of the large-scale *SSH* that contribute to the ocean pressure gradient.

2.3 ALTIMETER SSH MEASUREMENTS

The ability to measure sea level from satellites has evolved from the *Skylab* and *GEOS-3* satellites to the present day (Table 2-1), and developments continue to improve the quality as well as the range of studies to which the observations are applied. The largest factor affecting applicability is system errors. Since the first satellite altimeters, errors have been reduced several orders of magnitude. Thus, much more subtle changes within the ocean are now detectable, and the data allow a greater array of processes to be examined.

Satellite	*Begin*	*End*	*Ionosphere correction*	*Water vapor correction*	*Orbit inclination and altitude (km)*	*Repeat period (days)*	*Ground track separation (km)*
Skylab	May 1973	Dec 1973	Model	Model	50° 438 km	Nonrepeat	
GEOS-3	April 1975	Dec 1978	Model	Model	115° 843 km	37	80
SeaSat	June 1978	Oct 1978	Model	Radiometer	108° 790 km	Various	
Geosat Geodetic Mission	Mar 1985	Sep 1986	Model	Model	108° 785 km	Nonrepeat	
Geosat Exact Repeat Mission	Nov 1986	Jan 1990	Model	Model	108° 785 km	17.05	164
ERS-1	July 1991	Sep 1995	Model	Radiometer	98° 780 km	3, 35, 168	930, 80, 16
TOPEX/ Poseidon	Aug 1992		Dual Frequency Altimeter	Radiometer	66° 1,335 km	9.95	315
ERS-2	Aug 1995		Model	Radiometer	98° 780 km	35	80
GFO	Nov 1999		Model	Radiometer	108° 785 km	17.05	164
JASON-1	Jan 2002		Dual Frequency Altimeter	Radiometer	66° 1335 km	9.95	315
ENVISAT	Feb 2002		Dual Frequency Altimeter	Radiometer	98° 780 km	35	80
NPOESS	2013		Dual Frequency Altimeter	Radiometer			

Table 2-1 Altimeter missions have improved accuracy over time by incorporating information from supporting sensors such as dual-frequency altimeters for correction of the ionosphere total electron content and water vapor radiometers for correction of total water vapor. The range of orbit inclination, repeat period, and zonal ground track separation at the equator reflects the wide range of altimeter applications. The begin and end dates indicate the time period spanned by the returned data, not necessarily the launch or decommission dates.

In addition to the accuracy improvements, experience in working with the data has provided a diversity of techniques for separating possible errors from true sea level changes. The combination of observations with complex numerical models has allowed further separation of ocean processes from noise by constructing solutions that match both the observations and prescribed dynamical equations.

The altimeter instrument itself has been developed to provide an accurate measurement of the transit time of a radar pulse emitted by the satellite, reflected by the ocean surface, and returned to the satellite. Several techniques are used within the satellite hardware to allow a small ocean footprint simultaneously with a small transmitter/receiver antenna and a low power requirement. The intent within this chapter is to examine the altimeter measurement application to observing the ocean, so we do not pursue the details of the hardware and radar signal processing. The reader is referred to the material by Chelton et al. (2001), which provides a thorough analysis and treatment of this subject. The altimeter measurement is intended to represent an area larger than wind-driven waves and ocean swell but smaller than typical large-scale ocean features ranging from twenty to thousands of kilometers. The radar pulse footprint varies in size depending on the satellite altitude and the ocean wave height. The higher ocean waves reflect the radar pulse further from the subsatellite point. In calm seas, the ocean area reflecting the radar pulse has a diameter of about 3 km, and this increases up to 10 km in areas with waves of 15-m amplitude for the TOPEX/Poseidon altimeter. This is the across-track footprint size. Temporal averaging causes the footprint to be elongated in the along-track direction.

The quantity measured by the altimeter instrument is the radar propogation time that is converted to range (R, Figure 2-1), assuming a constant propogation speed of the radar pulse. This range must be corrected for effects on the radar pulse propagation speed and the reflecting surface roughness. The corrected satellite range together with satellite orbital height above the reference ellipsoid (O) provides the sea level height above the reference ellipsoid (SL)

$$SL = O - \left(R + A\right) \tag{2-10}$$

where A represents corrections to the measured range. For oceanographic purposes, the sea surface height above the ocean rest state (SSH) is of importance. If G is the geoid height above the reference then

$$SSH = O - (R + A) - G \tag{2-11}$$

Often the geoid height is unknown or contains substantial errors. These errors may be avoided by examining only sea level changes from one time to another or deviations from a long time period mean. The sea surface height anomaly ($SSHA$) is

$$SSHA = SSH - MDH = SL - (G + MDH) \tag{2-12}$$

where MDH is the mean dynamic height or height above the geoid due to the time-averaged ocean circulation.

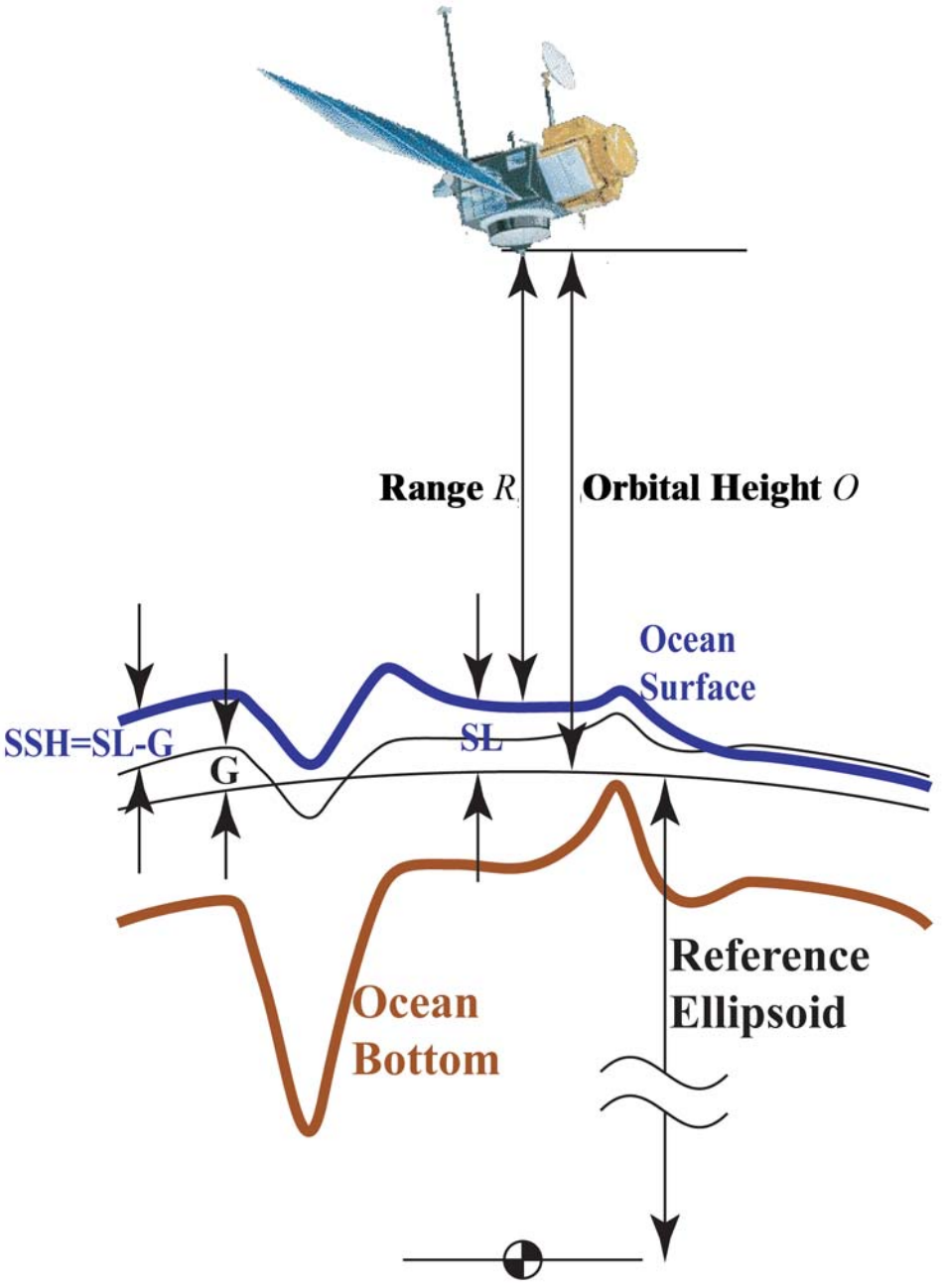

Figure 2-1 The altimeter measures the range (*R*) between the satellite and ocean surface by measuring the round-trip travel time of a radar pulse. Knowledge of the satellite distance (*O*) relative to the reference ellipsoid allows computation of the sea level (*SL*), and knowledge of the geoid (*G*) provides the sea surface height (*SSH*). Courtesy: Gregg Jacobs.

Within altimeter data sets, usually the altimeter range is provided assuming that the medium has no effect, and corrections to the range are provided. These corrections are represented by the variable *A* in Equation 2-10. The major atmospheric corrections are the dry troposphere, wet troposphere, and ionosphere corrections. The dry troposphere correction accounts for changes in propagation speed due to the total dry air mass. The total air

mass is obtained from surface pressure and is reliably estimated by global numerical weather prediction systems. The wet troposphere correction accounts for the total precipitable water effect on propagation speed. The spatial scales over which the water vapor content changes are relatively small, and small errors in weather prediction systems can lead to large errors in altimeter range. A majority of satellite altimeter instruments incorporate a water vapor radiometer to measure the water vapor content, which provides an accurate propagation delay correction. The ionospheric correction accounts for path delays due to the total electron count (TEC) below the satellite. Several methods have been used to measure the path delay due to ionospheric effects. The TOPEX altimeter measures range at two frequencies, each of which is affected differently by the TEC, thus providing a TEC measurement (Fu et al. 1994). Other techniques include DORIS, which measures the TEC between the satellite and ground stations. Using the TEC computed by GPS signal measurements, global ionospheric maps are also constructed for satellites that have no onboard method of measuring the TEC.

An accurate measure of distance from the ocean surface to the satellite is of little consequence without accurate positioning of the satellite relative to fixed reference surface. Usually, the fixed surface is the TOPEX/Poseidon reference ellipsoid defined as having a semi-major axis of 6378136.3 m and a flattening of 1/298.257. The satellite position relative to the reference ellipsoid must be known with accuracy better than the amplitude of the ocean signal of interest. Orbit solution accuracy is very important to the application of altimeter data and has improved greatly since the first GEOS-3 and Skylab altimeters, which had solution errors on the order of 10 to 100 m and restricted the data applicability. Present radial orbit solution accuracy for the *TOPEX/Poseidon* satellite is 2-cm RMS. This high accuracy is a result of improved satellite orbit solution techniques, improved models for the Earth's gravity field, and improved methods for observing satellite position. In spite of the relatively extreme orbit solution errors prior to the TOPEX altimeter mission, several very clever techniques were devised to mitigate the error impact by taking advantage of the error characteristics. Orbit solution errors are concentrated mainly at a frequency of one cycle per satellite revolution (referred to as 1 cycle per rev, or 1 cpr) with diminishing amplitude peaks concentrated around integer multiples of 1 cpr. Ocean features much smaller than these orbit error wavelengths are well separated. However, for the more subtle problems of climatic ocean circulation change, signals are large scale. Thus, early mission orbit solution errors prohibit their examination.

As discussed above, one method for removing geoid errors is by examining *SL* changes or deviations from a mean. For this method (referred to as collinear analysis), the satellite orbit is constrained to repeat within 1 km of a predefined ground track. For studies of the Earth shape, a few altimeter satellites, such as the Geosat Geodetic Mission, have been placed in non-repeating orbits. Geosat was originally a classified Navy mission to measure the marine geoid at a high spatial resolution, but the data were subsequently released after the ERS-1 geodetic mission, which was located in a 168-day repeat ground track. There is a wide range of possible exact repeat orbits, but three orbits have dominated for a range of reasons. The 17.05-day repeat orbit was occupied by *SeaSat* for a short time and then again after the *Geosat* satellite was moved from its Geodetic Mission to its Exact Repeat Mission. The *Geosat Follow-On* satellite also occupies the 17.05-day repeat orbit. One objective of *SeaSat* and *Geosat-ERM* was to sample the ocean mesoscale, which has spatial scales on the order of 20 to 300 km, and the 17.05-day repeat orbit is well suited for this. The European Remote Sensing satellite *ERS-1* was moved between several different sun-synchronous repeat orbits. A 3-day repeat orbit was used for high latitude ice studies, a 35-day repeat orbit was used for general studies, and a 168-day repeat orbit was used for geodetic studies. The *ERS-2* satellite was held to a 35-day repeat orbit throughout its lifetime for

general studies. Both the *Geosat* and *ERS* satellites were at about 780-km altitude. The TOPEX/Poseidon mission repeat period is 9.95 days. The choice was based on the desire for a higher altitude (1,300 km) to minimize atmospheric drag effects on orbit solution errors, and a repeat time that would carefully alias the major ocean tide signals to frequencies that would be resolvable from the annual and semiannual over the planned mission life. The tide aliasing problem can be quite severe. If ocean tides are aliased to frequencies at which significant energy exists from other ocean variations (such as at the annual frequency), then either errors are induced in the observations of the tides due to the ocean variations, or errors are induced into observations of the ocean variations due to the tide aliases. Tide alias problems hampered many studies using the Geosat-ERM and ERS data sets until higher accuracy tide solutions were constructed using the TOPEX/Poseidon data sets.

The orbit parameters are chosen to best observe the features of importance to the particular mission. The wide range of orbit parameters reflects the wide range of processes that have been observed by the altimeters. The track separation given in Table 2-1 is the distance along the equator between parallel tracks. Away from the equator, the zonal distance between tracks decreases to 0 at the maximum latitude of the observations. The latitudinal extent of the observations is related to the orbit inclination (angle between the equatorial plane and the orbit plane) given in Table 2-1. Note that there is also a relation between the ground track spacing and the repeat period. As ground track spacing is decreased the repeat time increases. The product of ground track spacing and repeat period is a constant for a selected altitude.

2.4 GEOID HEIGHT G

If the oceans were at rest and no forcing were applied, then the ocean surface would lie on the geopotential surface referred to as the geoid. The height of the geoid above the reference ellipsoid varies from -80 to 100 m across the globe, and the geoid spatial gradients are generally greater than the *SSH* spatial gradients caused by ocean flow. One example of the marine geoid is provided by the EGM96 geoid solution (Figure 2-2a). The observed and modeled contributions of ocean circulation to *SSH* are much smaller than that of the geoid (Figures 2-2b, 2-2c, 2-2d).

Much geoid information has been gained from gravimetry measurements over land, onboard ships, and by aircraft. Land gravimetry data are dense while marine gravimetry observations are relatively sparse. The marine geoid itself has several important applications (Sandwell 1991), which include understanding spreading ridges, subduction zones, and hot spots that are all apparent within the satellite-observed geoid.

Because early altimeter (GEOS-3 and Skylab in particular) missions were relatively short lived and contained large errors, the missions concentrated at first on observing the largest sea level signal, which is the geoid. The ocean deviation from its rest state is much smaller than the geoid height above the ellipsoid and is usually considered to be noise for geoid studies. At the time of *GEOS-3* and *Skylab*, the geoid signal had not been directly observed, and so the results were quite staggering (Marsh and Martin 1982; Freedman and Parsons 1986). Many years after each altimeter mission, reprocessing of the data and recomputation of orbit solutions and other correction values have led to much improved data that are more valuable for both geoid and oceanographic studies.

The Earth geoid on large scales is represented through spherical harmonic expansion coefficients of the gravity field. The coefficients are solved through inverse methods that join surface gravimetry, satellite position, and satellite altimetry observations with dynamical models of satellite movement. For example, the Joint Gravity Model (JGM) used for

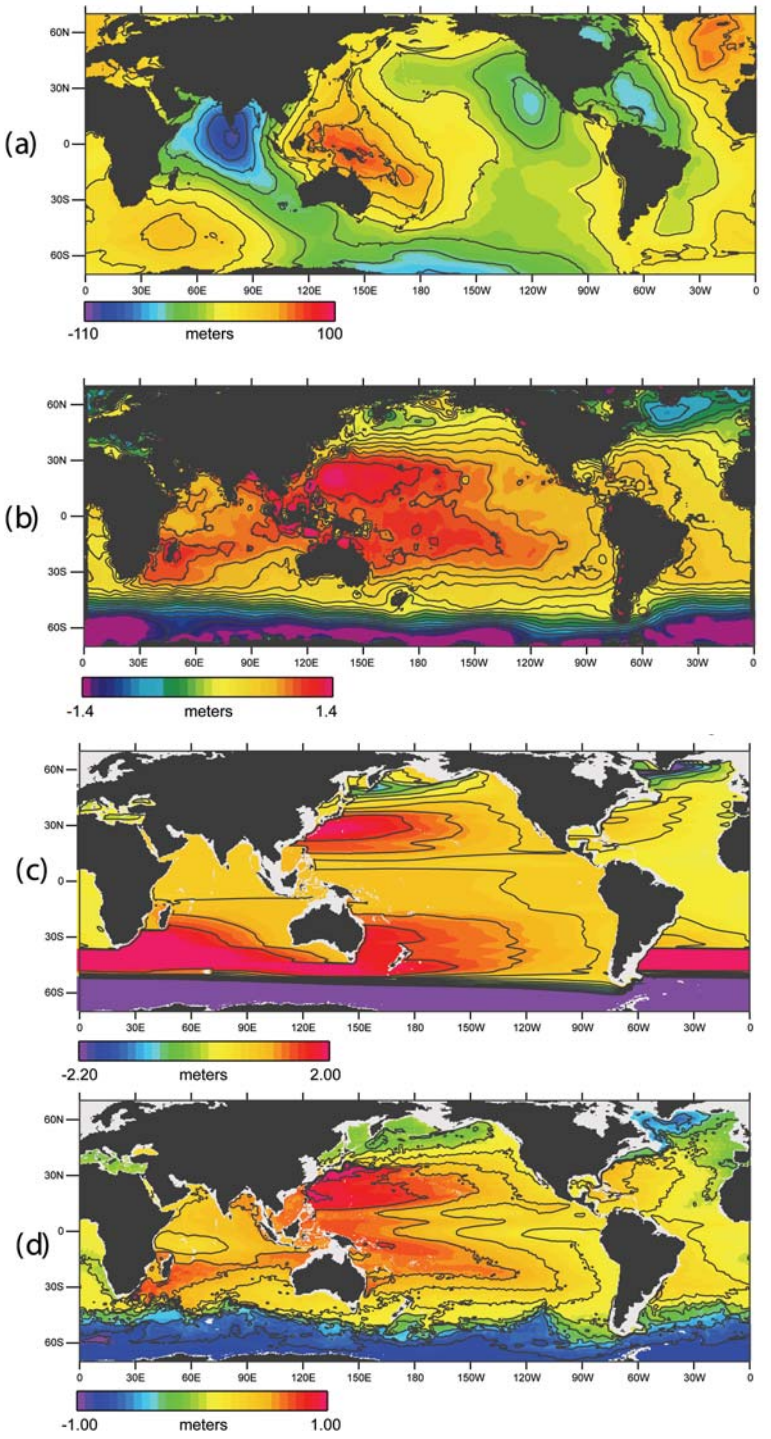

Figure 2-2 The ocean geoid (a) is the height above the reference ellipsoid the ocean would follow if there were no flow or forcing. The mean *SSH* above the geoid (b) has been determined most accurately by the *TOPEX/Poseidon* satellite. The linear ocean circulation response to wind stress (c) provided by a numerical solution to dynamical equations indicates relatively good agreement with the observations. The nonlinear ocean interactions (d) provide substantial changes in some areas, particularly the southern ocean. Courtesy: Gregg Jacobs from data provided by C. K. Shum, Yuchan Yi, E. Joseph Metzger, and Ole Martin Smedstad

TOPEX/Poseidon is based on a spherical harmonic expansion to degree 70 (Nerem et al. 1994). The EGM96 geoid presented in Figure 2-2a is based on a degree and order 360 expansion. The true geoid field contains structures having much smaller spatial scales than the degree and order 360 gravity model may resolve. Present satellite missions to provide gravity measurement at smaller spatial scales include the CHAllenging Minisatellite Payload (CHAMP) and the Gravity Recovery and Climate Experiment (GRACE), which are providing information to form a geoid applicable for oceanographic purposes with length scales down to 200 km. Below this scale, substantial variations are expected to remain in the marine geoid, caused by ocean trenches, seamounts, and other small-scale mass anomalies below the ocean surface.

The non-repeat altimeter missions provide a large data store for short-scale gravity and geoid observations. The data obtained by *ERS-1* during the 168-day repeat geodetic mission (April 1994 through March 1995) in combination with Geosat geodetic mission data (March 1985 through September 1986) provide an enormous increase in the spatial resolution of sea level and slope measurements.

Several methods have been devised to examine short-scale gravity variations. One method (Sandwell and Smith 1997) uses the measured sea level gradients in the direction along the satellite ground track to construct the gravity anomaly and geoid heights at points across the Earth's surface. The gravity anomaly $\Delta g(\mathbf{x})$, geoid $G(\mathbf{x})$, and gravitational potential $V(x)$ are closely related. The gravity anomaly is related to the gravitational potential at the geoid surface by

$$\Delta g(\mathbf{x}) = -\frac{\partial V(\mathbf{x})}{\partial z} \tag{2-13}$$

where $\mathbf{x}$ is the position along the geoid surface and z is the height above the surface.

When examining only the deviations from the large-scale global gravity field (such as deviations from the EGM96 gravity field), the geoid and gravitational potential are related through Brunt's formula

$$G(\mathbf{x}) \cong \frac{1}{g_o} V(\mathbf{x}) \tag{2-14}$$

Thus a construction of gravity anomaly may be related to the geoid on short spatial scales. The altimeter provides measurements of the geoid gradient in the direction along the satellite ground track (measurements in which the ocean circulation effects are considered noise).

Following Sandwell and Smith (1997), the altimeter-measured along-track *SL* gradients provide measurements of eastward and northward geoid deflection [$\eta(x)$ and $\xi(x)$] that are related to the geoid and gravitational potential by

$$\eta(\mathbf{x}) \equiv -\frac{\partial G}{\partial x} \cong \frac{-1}{g_o}\frac{\partial V}{\partial x} \tag{2-15}$$

$$\xi(\mathbf{x}) \equiv -\frac{\partial G}{\partial y} \cong \frac{-1}{g_o}\frac{\partial V}{\partial y} \tag{2-16}$$

Since the gravitational potential is a Laplacian field

$$\frac{\partial^2 V}{\partial x^2} + \frac{\partial^2 V}{\partial y^2} + \frac{\partial^2 V}{\partial z^2} = 0 \tag{2-17}$$

the combination of Equations 2-13, 2-15, 2-16, and 2-17 provides the vertical gravity anomaly gradient relation to the altimeter *SL* gradient measurements

$$\frac{\Delta g}{\partial z} = -g_0 \left(\frac{\partial \eta}{\partial x} + \frac{\partial \xi}{\partial y} \right) \tag{2-18}$$

Ocean gravity anomalies (which lead to geoid deformations) are a result of density anomaly features such as seamounts or trenches on the sea floor. One example of the mean and associated gravitation demonstrates the large variations that may occur over short distances (Figure 2-3). These types of examinations have led to a better understanding of the relation between the seafloor spreading rate and seafloor topographic roughness (Smith 1998). For example, the spreading rates of the continental plates at the Atlantic mid-ocean ridge are much less than that in the Pacific ridge. The end effect is that the ocean floor roughness (amplitude and abundance of seamounts) is greater in the Atlantic Ocean than the Pacific.

Presently, the geoid is known with accuracies of about 10 cm on spatial scales greater than 1,000 km. On spatial scales of ocean features of 20 km, the geoid errors are much larger than the ocean signal. For example, in Figure 2-3, the *SL* changes by about 100 m over 4,000 km. A 20-km change in position thus leads to about 50-cm change in height, which is of greater magnitude than the *SSH* change caused by ocean circulation throughout most of the world's oceans. On smaller spatial scales, the gradients in Figure 2-3 can be much greater. The *SL* is not presently well-known on spatial scales less than about 1,000 km. However, if we are interested in the sea level change from one time to another or the sea level deviation from the mean, then the geoid is inconsequential. The sea level height above the reference ellipsoid may be differenced between two subsequent measurements to provide the sea level change between the times, or sea level deviations from the observed mean sea level over a long time period may be used. This is presently one of the widespread methods for using altimeter data and is referred to as repeat or collinear analysis.

In order to use collinear analysis with altimeter data, the satellite is generally constrained to an exact repeat orbit. That is, mission planners actively control the satellite to insure that the sub-satellite point does not deviate more than 1 km from a predefined reference ground track. The 1-km requirement is a result of geoid gradients in the direction perpendicular to the ground track. As may be observed from Figure 2-3, the mean *SSH* height changes by about 100 m over 4,000 km. The gradient implies a 1-km deviation of the satellite from its reference ground track leads to a 2.5-cm difference in *SSH*. This could be misconstrued as oceanographic circulation change. By restricting the satellite to 1 km of a reference ground track, the variations induced through the combination of geoid gradient in the direction perpendicular to the ground track and the small variations in the sub-satellite point from one repeat pass to the next produce effects in the sea surface height variability that are typically much less than the expected oceanographic variations (Brenner et al. 1990). Knowledge of the geoid gradients from geodetic altimeter missions has provided significant reduction in this error source, and, in the future, dedicated gravity missions such

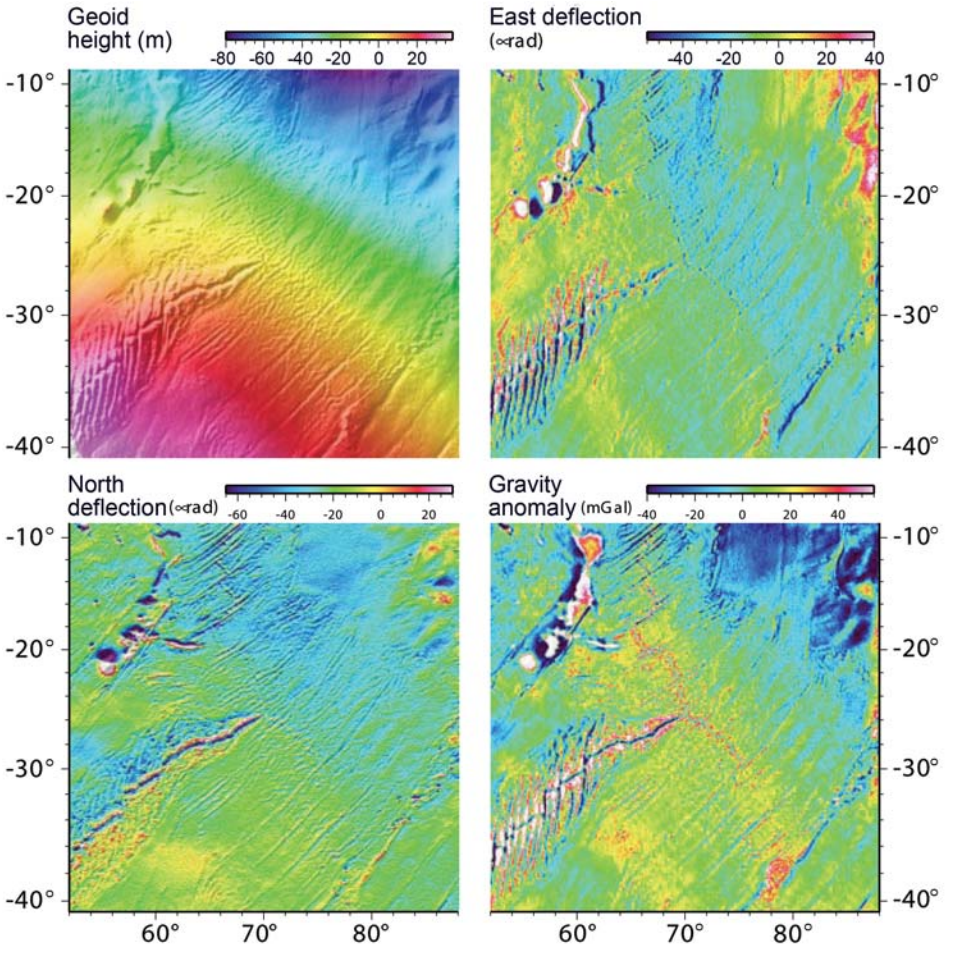

Figure 2-2 The ocean geoid (a) is the height above the reference ellipsoid the ocean would follow if there were no flow or forcing. The mean *SSH* above the geoid (b) has been determined most accurately by the *TOPEX/Poseidon* satellite. The linear ocean circulation response to wind stress (c) provided by a numerical solution to dynamical equations indicates relatively good agreement with the observations. The nonlinear ocean interactions (d) provide substantial changes in some areas, particularly the southern ocean. Courtesy: Gregg Jacobs from data provided by C. K. Shum, Yuchan Yi, E. Joseph Metzger, and Ole Martin Smedstad

as CHAMP and GRACE are expected to provide accurate geoid solutions down to 200 km. Thus while collinear analysis will still be a powerful technique, its necessity will probably decrease over time.

2.5 TIDES

The longest-studied ocean process is tides. The earliest predictions of tides were based on long time period observations of sea level along with the observation that tides are periodic. The dynamics and forcing of tides were not known, and predictions were possible only at observation points. Through the work of Newton and Laplace, the dynamics and forces controlling tides have been revealed. Gravitational and centripetal forces produce tides. The primary two bodies generating tidal forces are the moon and sun, with the sun gravitational attraction amplitude about 46% of the moon. Other gravitational forces are negli-

gible. The movements of the sun and moon and thus forcing of tides are predictable with a high degree of accuracy. This makes tides one of the most predictable ocean processes. Today understanding tides and their controlling dynamics is vital for coastal management and determining the environmental impact of proposed coastal changes.

Understanding the forcing that generates tides helps to better understand the global tide structure. The forcing is most easily expressed as the gradient of a potential function. The tide-generating potential at a point on the Earth's surface at distance r from the Earth center due to moon of mass M at a distance of R from the Earth center is approximated as (Apel 1987)

$$\Phi = -\frac{GM}{R}\frac{1}{2}\left(\frac{r}{R}\right)^2\left(3\cos^2\gamma - 1\right) \tag{2-19}$$

where γ is the angle between the vector from the Earth center to the point on the Earth and the vector from the Earth center to the moon center. A similar potential is generated by the sun. Time variations in the tide potential are induced as the angle γ changes (due to the Earth rotation, the relative position of the sun and Earth, and the relative position of the moon and Earth). For a point on the Earth at latitude ϕ, with the moon at a declination angle ϕ_m above the equatorial plane and at a longitude (or hour angle) of θ_m

$$\cos\gamma = \sin\phi\,\sin\phi_m + \cos\phi\cos\phi_m\cos\theta_m \tag{2-20}$$

The tide potential is then

$$\Phi = \frac{GM}{R}\frac{1}{4}\left(\frac{r}{R}\right)^2\left[\begin{array}{l}\left(3\sin^2\phi - 1\right)\left(3\sin^2\phi_m - 1\right) + \\ 3\sin 2\phi\sin 2\phi_m\cos\theta_m + \\ 3\cos^2\phi\cos^2\phi_m\cos 2\theta_m\end{array}\right] \tag{2-21}$$

The first term within the brackets varies in time as the lunar declination angle ϕ_m changes and provides a slowly changing variation as the moon orbits the Earth. The second term provides a 1 cycle per day variation (or diurnal variation from $\cos\theta_m$) and the third term provides a 2 cycle per day variation (or semidiurnal variation from $\cos 2\theta_m$). Both the diurnal and semidiurnal tides are modulated by the more slowly changing declination. The complex modulation of the diurnal and semidiurnal tides by the changing declination may be simplified to a large degree. Doodson (1922) demonstrated that the diurnal and semidiurnal terms may be expanded in a Fourier series, with each term of the expansion containing a different frequency that is an integer combination of six basic frequencies. The six integers are the Doodson numbers and provide a unique number for each tide constituent. In this way, each tide constituent is viewed as having a single fixed frequency.

Note that Equation 2-21 provides the tidal potential for only the moon. The tidal potential generated by the sun is identical in form. The frequencies of solar tides are different from the lunar tides due to the solar declination.

Spatial variations in the tide-forcing potential depend only on latitude, with the diurnal tides having larger amplitudes near 45° latitude and semidiurnal tides having larger amplitudes near the equator. Since the forcing is periodic in time, if the ocean dynamics were linear then the ocean response would be expected to be periodic in time. Largely this is true

for tides, though deviations do occur on the continental shelf due to nonlinear interactions. The ocean response to the tide forcing is strongly dependent on the basin geometry and bathymetry (Figure 2-4). In most regions throughout the globe, tides are the largest contributors to the sea level variability. Understanding tidal variations is important to determine the dissipation of energy input to the oceans from the gravitational forcing. The energy dissipation is critical to determine the angular momentum changes of the Earth, and thus changes to the Earth rotation speed.

Researchers have substantially improved numerical tide models in the past decade. Models representing the pertinent ocean dynamics and forced by the tide potential (first-principle models) are able to account for a large fraction of the tidal variability in the deep ocean. However, the models have inherent errors due to the resolution afforded by present-day computers. In addition, much of the world ocean depth has not been measured at sufficiently high resolution and accuracy. The lack of ability to represent the equations of motion on computers and lack of knowledge of the ocean geometry lead to errors in numerical tide models. The Geosat-ERM aliased Schwiderski (1980) tide solution errs both in time and space. Tide errors appeared to be propagating oceanographic features (Schlax and Chelton 1994). Improvements in tide solutions solved this problem, but residual tide errors now contaminate the study of much more subtle processes such as climate change.

Tide modelers have used observations to improve the accuracy of tide solutions. The tide solutions of Schwiderski (1980) used information from tide gauge stations across the globe. However, the relative scarcity of measurement points did not improve solution accuracy to sufficient levels. The TOPEX/Poseidon repeat period was chosen in part because of its favorable tide alias characteristics. Unlike the Geosat-ERM, which aliased tides to appear nearly as oceanographic features, the TOPEX/Poseidon sampling pattern was designed to prevent this effect. The result is not only that tides do not significantly influence most oceanographic features, but also the oceanographic features do not significantly influence tide estimates obtained from the satellite data. Thus the satellite data from *TOPEX/Poseidon* has been very successful in improving tide estimates by assimilating the data into numerical models (Le Provost et al. 1998; Shum et al. 1997).

2.6 MEAN BASIN-SCALE CIRCULATION

The *TOPEX/Poseidon* altimeter satellite is the first to provide data of sufficient accuracy to directly examine the *SL* deviation from the geoid on basin scales (sizes of the Atlantic and Pacific Ocean basins). As an example of the ocean circulation revealed by the altimeter, the mean TOPEX/Poseidon *SSH* above the EGM96 geoid (Figure 2-2b) is compared to the mean *SSH* resulting from a numerical ocean model forced by wind stress (Figures 2-2c and 2-2d). The geostrophic equations (Equations 2-8 and 2-9) imply ocean currents flow along lines of constant sea level with circulation rotating clockwise about high *SSH* areas and counterclockwise about low *SSH* areas in the northern hemisphere. The circulation flows in the opposite direction in the southern hemisphere due to the change in sign of the Coriolis parameter *f*.

The circulation features apparent in the TOPEX/Poseidon mean *SSH* are filtered so that only large length scales remain. The length scales removed are based on the amplitude of errors in the geoid and the amplitude of expected ocean features at the same spatial scales. Only wavelengths at which the expected geoid errors are much smaller than the expected *SSH* signal are included. As future gravity missions reduce geoid errors, the spatial scales that may be included in the derived mean circulation may be decreased. At present, the major ocean circulation gyres are apparent.

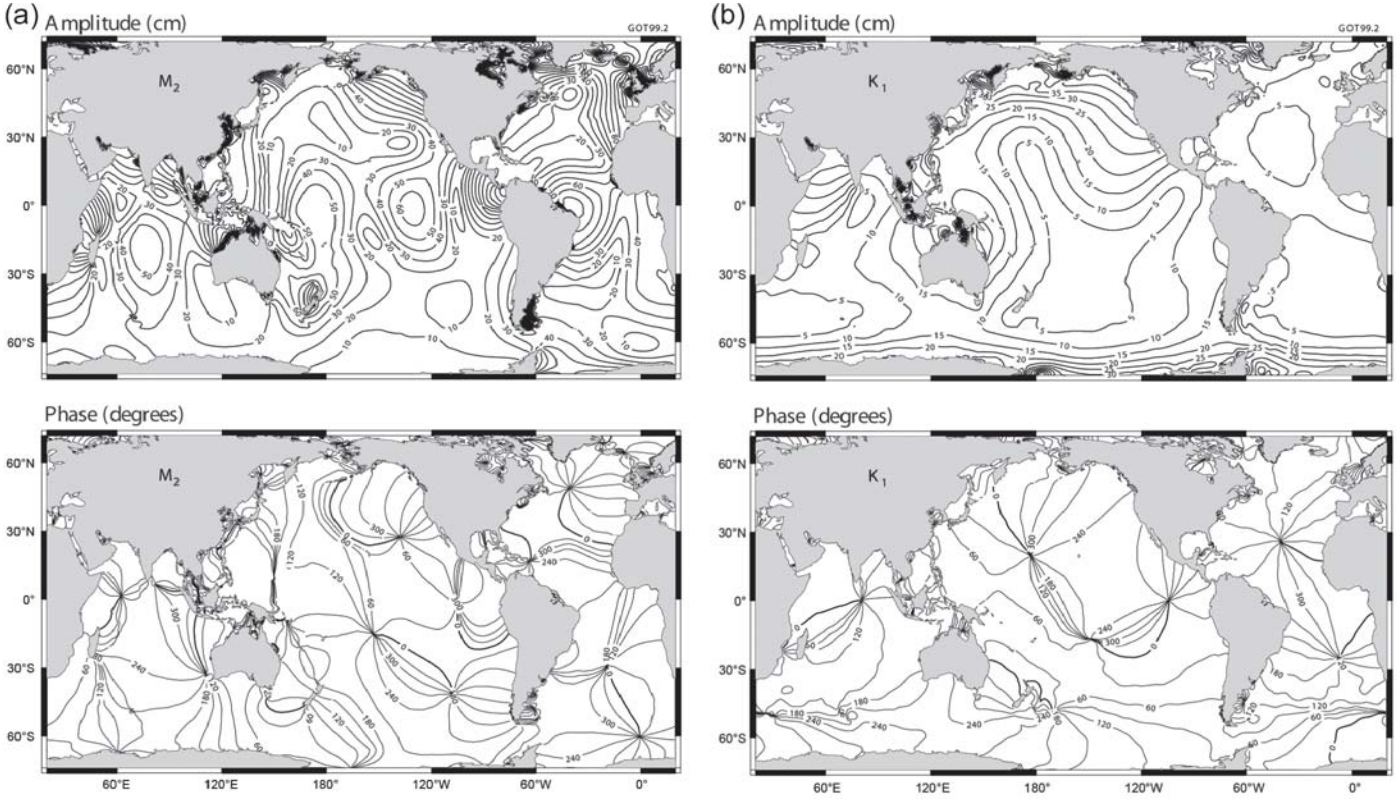

Figure 2-4 The total tide height at a point is the sum of all the constituents. Here we present the primary (a) semidiurnal constituent M2 and (b) diurnal constituent K1 solutions. The primary diurnal tide-forcing component has largest amplitudes at 45°, and the primary semidiurnal tide-forcing component has largest amplitudes at the equator. However, the ocean response is strongly affected by the land masses. The tide of each constituent at a particular point is $a\ cos(\omega t + \phi)$, where a is the amplitude, ω is the tide frequency and ϕ is the tide phase. The points at which the phase lines meet are amphidromes where the tide amplitude is zero. Courtesy: Richard D. Ray.

For example, the North Atlantic circulation appears in both the TOPEX/Poseidon and numerical model results; the circulation appears as a positive *SSH* across the Atlantic Ocean between the equator and 35°N along with a low *SSH* in the northern Atlantic. The positive *SSH* implies an anti-cyclonic circulation. This gyre forms a northward-flowing western boundary current along the North American coast. The western boundary current separates from the coast as the Gulf Stream and subsequently flows eastward into the central Atlantic. A similar circulation system is set up in the North Pacific with the subtropical gyre forming the Kuroshio Current separating from the Japan coast and flowing eastward into the Pacific basin. Within the south Atlantic and Pacific Oceans, subtropical gyres form along with western boundary currents that separate and propagate into the ocean interiors.

The cause of the large-scale gyre circulations is related to the wind stress. The ocean surface communicates with the atmosphere through wind stress, heat flux, evaporation, and precipitation. A perturbation expansion of the momentum equations is carried out in Pedlosky (1979). The perturbation expansion provides the geostrophic equations (Equations 2-8 and 2-9) as the first-order balance, and second-order balance provides the quasi-geostrophic (QG) equations. The steady-state linear ocean response to wind stress given by the QG equations is

$$\frac{\partial h}{\partial x} = curl(\tau) \tag{2-22}$$

where τ is the wind stress vector. That is, in an area of negative wind stress curl, the *SSH* should decrease toward the east. This simple response to wind stress curl is referred to as the Sverdrup flow. A numerical model provides an example of the ocean linear response to the wind stress (Figure 2-2c). The true ocean contains large deviations from the Sverdrup solution, particularly in the Southern Ocean encircling the Antarctic continent. A large eastward-flowing current appears across the Southern Ocean in the linear results. This current is much stronger than actually observed. The disagreement occurs because the linear model lacks dynamical processes that act to reduce the strength of the current. In particular, nonlinear mesoscale eddies act as turbulence to diffuse momentum (as well as heat and salinity). When nonlinear processes are included in the numerical model the comparison with the altimeter observations improves markedly (Figure 2-2d). The nonlinear mesoscale variability is discussed further in Section 2.8.

2.7 WIND-DRIVEN BAROTROPIC VARIABILITY

A description of the vertically averaged motion is obtained by integrating the momentum equations (Equations 2-2 and 2-3) from the ocean bottom to the surface (Csanady 1984). The governing momentum equations are

$$\frac{\partial U}{\partial t} - fV + gD\frac{\partial h}{\partial x} = \frac{1}{\rho_o}\tau_x \tag{2-23}$$

$$\frac{\partial V}{\partial t} + fU + gD\frac{\partial h}{\partial y} = \frac{1}{\rho_o}\tau_y \tag{2-24}$$

where *D (x,y)* is the total water depth, *(U,V)* is the vertically integrated velocity, and (τ_x,τ_y) is the wind stress acting on the ocean surface. The influence of nonlinear terms and bottom friction are ignored. Suppose a constant wind is applied to the ocean for a long time. Eventually the ocean reaches equilibrium so that the time rate of change is zero. In the absence of Coriolis force, according to Equations 2-23 and 2-24 the *SSH* gradient would be proportional to the wind stress. For a positive τ_y (a southerly wind stress or wind from the south) the sea level increases toward the north. The *SSH* gradient in response to the wind stress is proportional to 1/*D* so more shallow areas contain a larger *SSH* response than deeper areas. One extensive area over which we may examine the *SSH* response to wind stress is the Yellow and East China Seas between China and Korea. The average depth of this continental shelf is about 60 m compared to 3,780-m average depth throughout the global oceans (Pickard and Emery 1982).

Altimeter-measured *SSH* variations present an excellent opportunity to observe the behavior of the ocean in the continental shelf region where short time period response to wind stress dominates. Certainly, altimeter data implications are well understood in the open ocean where time scales are longer than the satellite repeat period, and this has been exploited in many studies to examine deep ocean circulation physics (Fu and Cheney 1995). The difficulty in shallower areas stems mainly from the lack of sufficient temporal sampling. The typical wind-forcing events across the Yellow and East China Seas have periods of less than one week. The circulation response time is on the order of one day (Hsueh 1988). It is not possible for a satellite altimeter to directly observe the *SSH* development throughout the time period of a wind-forced barotropic event. Instead, we may examine the ocean response to short time period forcing through statistical methods.

The wind forcing may be examined at the altimeter measurement times, which allows determination of the stochastic, or averaged, *SSH* response. For example, on average, what is the *SSH* response to a southerly 1 N/m^2 wind stress? If there are several observations of *SSH* and several simultaneous observations of the wind stress, the average *SSH* response can be calculated. The temporal sampling density is inconsequential as long as a sufficient number of wind events and their responses are observed. By examining the time- and space-lagged cross covariance of the *SSH* and wind stress, the response to the wind stress at earlier times and distant locations may also be examined. The transfer function provides the linearized response of ocean *SSH* to the wind stress

$$SSH(\mathbf{x},t) = \int_S \int_{t'=t-T}^{t} \mathbf{h}^{\mathrm{T}}(\mathbf{x},t,\mathbf{x}',t')\mathbf{W}(\mathbf{x}',t')\,dt'd\mathbf{x}' \tag{2-25}$$

The wind stress $\mathbf{W(x', t')}$ is a column vector at the position $\mathbf{x}'$ and time $\boldsymbol{t}'$. The function $\mathbf{h}^{\mathrm{T}}(\mathbf{x}, t, \mathbf{x}', t')$ is the two-element vector transfer function we wish to estimate. It provides the linear contribution of the westerly and southerly wind stress components at a position $\mathbf{x}'$ and time $\boldsymbol{t}'$ to the *SSH* at **x** and *t*. The transfer function $\mathbf{h}^{\mathrm{T}}(\mathbf{x}, t, \mathbf{x}', t')$ is optimally estimated by minimizing its expected error variance. This procedure leads to an eigen decomposition of the wind-stress covariance matrix into its most significant modes. The procedure then computes the *SSH* response to each wind stress mode.

In the northern Yellow Sea, one wind stress mode indicates the development of a northerly wind stress event (Figure 2-5a). The event contains an area of strong northerly wind stress that moves from the northwest to the southeast as a front pushes through the region. The time series of the mode amplitude indicates when this particular type of event typically occurs, which is in the winter as fronts move through the area from Siberia. The *SSH* re-

sponse to this mode is computed by a correlation of the *SSH* observed by the altimeter to the time series of the wind stress mode. The *SSH* response observed by the altimeter and a duplicate analysis performed on a numerical model of the region (Figure 2-5b) indicate similar response to the wind stress. The *SSH* response in the northern Yellow Sea is negative with *SSH* sloping up toward the south as would be expected from Equations 2-23 and 2-24. In addition, the *SSH* slopes up from the central Yellow Sea to the Chinese coast in both results. This response is relatively rapid, occurring over a time period of a day. Some of the differences in the observed and modeled results of Figure 2-5b are due to the confined model domain. That is, the total water mass within the model domain does not change, whereas in the true ocean there is a large water mass that moves into the open Pacific Ocean in response to the northerly wind bursts. In contrast to the continental shelf ocean response to the wind forcing, the deep ocean baroclinic variability is relatively slow to evolve. Because of this, it is possible to directly view the temporal development of the mesoscale field without resorting to such statistical procedures.

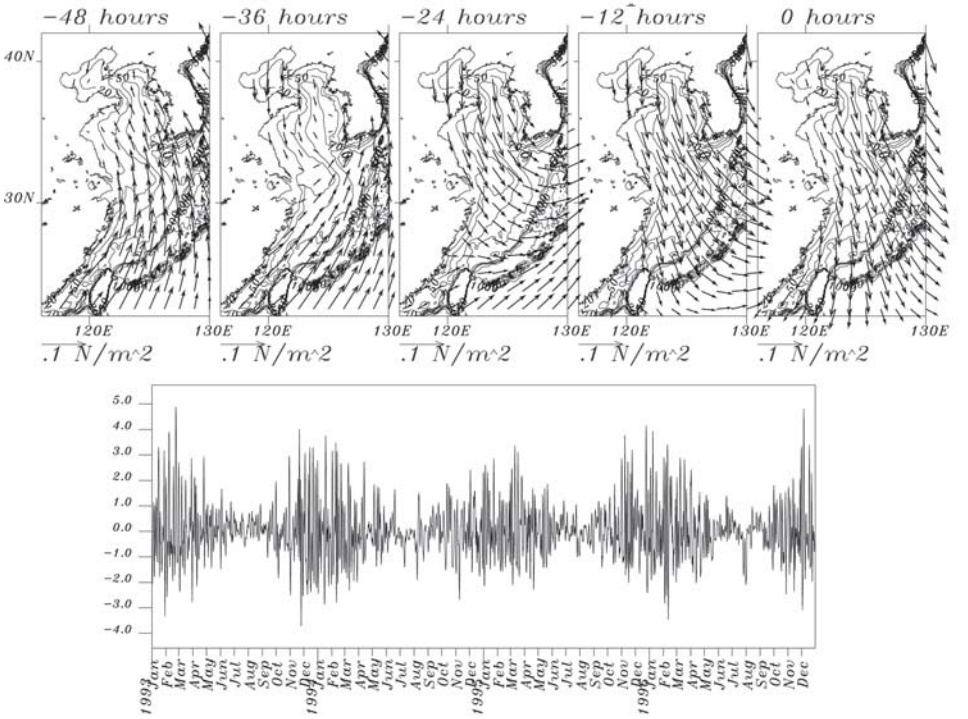

Figure 2-5a Wind stress is one of the principle drivers of ocean circulation. Based on historical data, one of the typical wind events through the Yellow and East China Seas area is the passage of Siberian fronts during winter. These wind events cause large northerly wind stress and propagate through the region from the northwest to southeast. The panels at the top indicate the typical development of one of these events over a 48-hour time period. The time series at the bottom indicates when these events have occurred from 1993 through 1996. Source: Jacobs 1998.

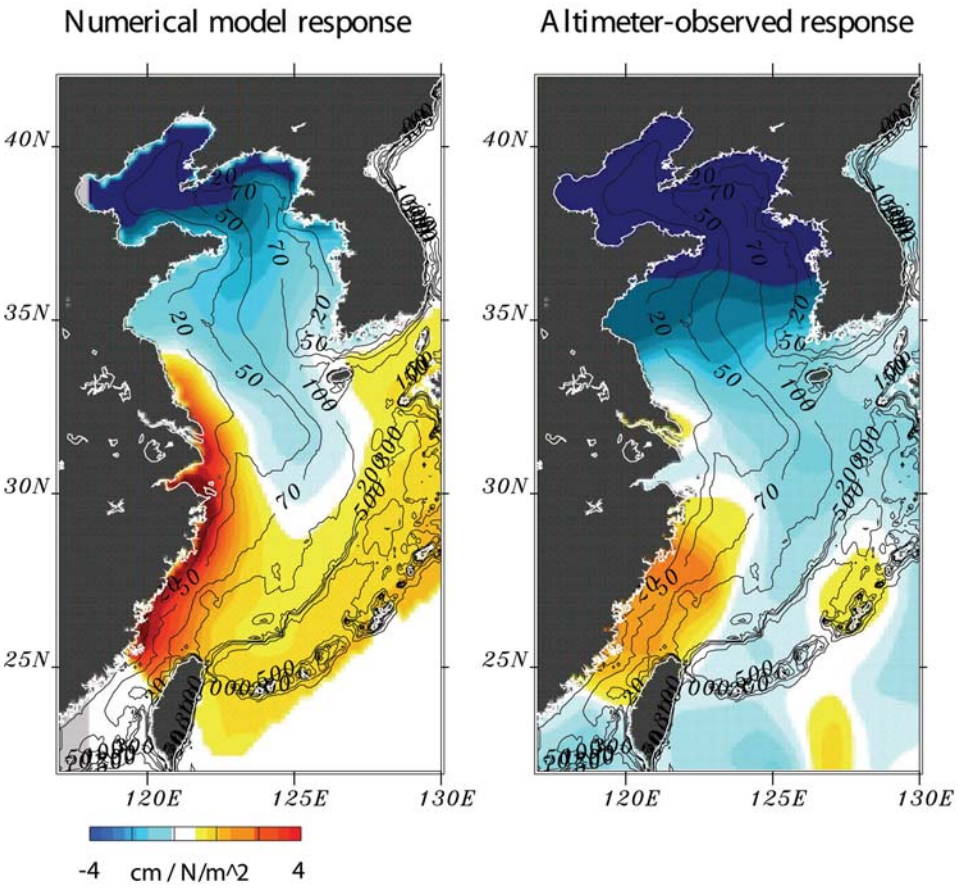

Figure 2-5b The response observed by the *TOPEX/Poseidon* satellite to the development of northerly wind stress indicates a sea level setdown in the northern Yellow Sea due to the northerly wind stress. The observed and barotropic-model results both contain the general setdown in the northern Yellow Sea as well as the setup along the Chinese coast. There is a difference in the mean *SSH* response, as the model is a closed domain without water mass exchange with the open Pacific Ocean. The contour lines indicate the ocean depth. Source: Jacobs 1998.

2.8 BAROCLINIC VARIABILITY AND THE MESOSCALE

A majority of the large-scale ocean circulation is forced by wind stress, and the sun provides the energy driving both the atmosphere and ocean circulation. The ocean and atmosphere act to transfer the high heat input at the equator to the high heat loss at the poles. The Gulf Stream and Kuroshio carry high-temperature water northward from the equator. However, only a portion of the heat transfer is accomplished by the mean flow. As is the case with many fluid processes, turbulence is a very efficient transfer mechanism. The large-scale ocean turbulence occurs in the form of ocean eddies that range in size from 20 km at high latitudes to several hundred km near the equator. Eddies can entrain warm water from the south of the Gulf Stream and Kuroshio and carry the water northward, or the eddies can entrain cold water from the north side of these currents and carry the water southward. Examinations of numerical ocean models indicate that 1/3 to 1/2 of the energy transport is through eddies (Jayne and Marotzke 2002). The model eddy activity in these studies is actually lower than observed; so the importance of the eddy transfer of energy is most probably higher than what is known through numerical models.

In addition to the importance to climate, eddies have an impact on day-to-day operations in the ocean. In a manner similar to atmospheric weather prediction, ocean mesoscale prediction provides information on currents and temperatures. Eddies create variations in the thermocline depth, which change water temperatures, alter biological processes, and influence fishing activities. Thermocline depth variations also change the spatial distribution of total heat in the ocean, which strongly influences the atmospheric predictions of hurricane development. Large currents are associated with eddies. Ships crossing the ocean can take advantage of favorable currents or avoid unfavorable currents to plot an optimal path and minimize fuel costs. Oil drilling operations in deep water must often be shut down in large currents. The mesoscale field has a large effect on many ocean activities, and providing real-time information on the ocean mesoscale circulation is important to many people.

The time periods over which eddies are generated, move through the ocean, and dissipate range from a week to years. Prior work undertaken only from ships was difficult and could not follow individual eddies for long time periods. Altimeter observations (Figure 2-6a) have allowed extensive examination of eddy life cycles (Schouten et al. 2000). Figure 2-6b provides one example of the mesoscale field for the Gulf Stream region in the North Atlantic. The field is a combination of TOPEX/Poseidon, ERS-2, and GFO observations through an optimal interpolation technique. The implied geostrophic velocity is also overlaid on the plot. The Gulf Stream flows northward along the North American coast to Cape Hatteras, North Carolina, where the stream separates and flows eastward into the Atlantic Ocean.

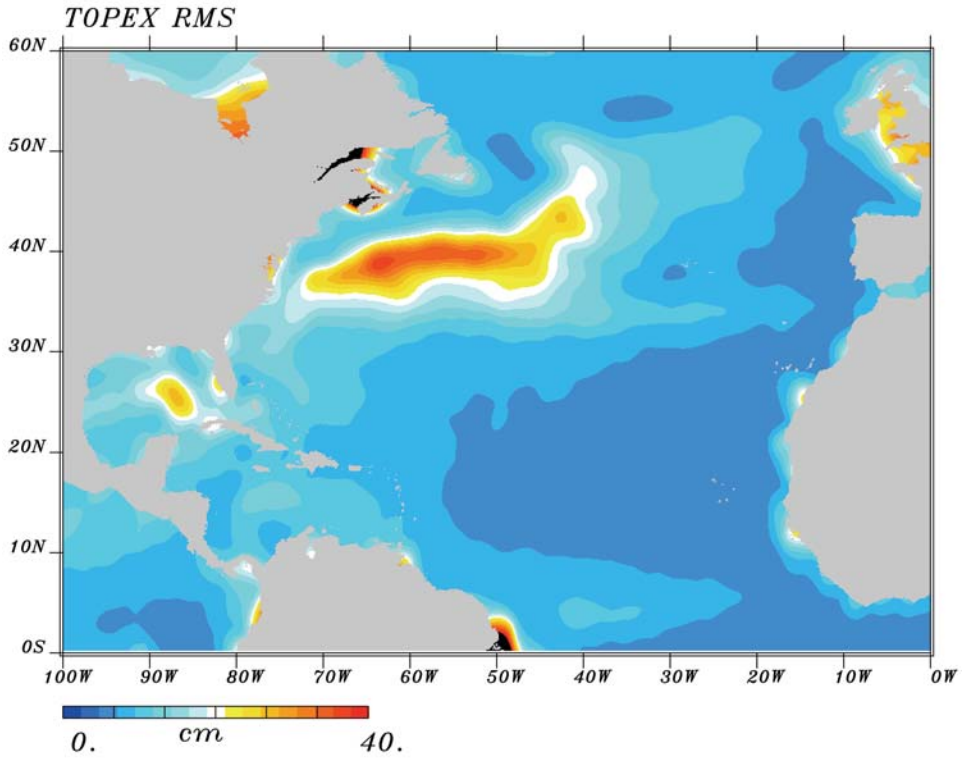

Figure 2-6a The RMS *SSH* variability measured by the TOPEX/Poseidon altimeter indicates that the largest variations occur in the intense western boundary currents and the eastward extensions into the ocean interiors. This variability is associated with mesoscale eddies, which are an instability process maintained by the energy available in the vertical shear of velocity. Courtesy: Charles N. Barron, Naval Research Laboratory.

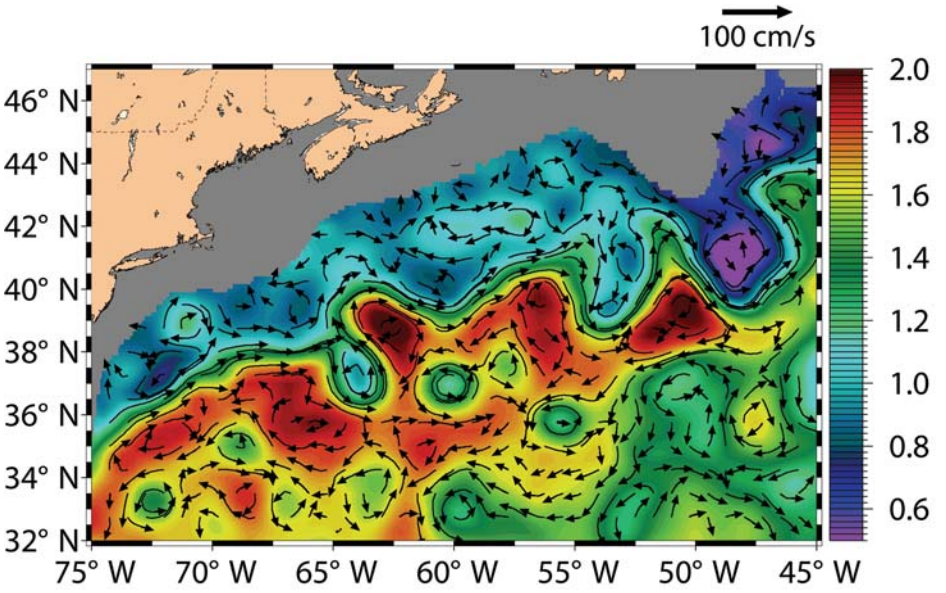

Figure 2-6b A sea level snapshot from 27 November 2001 indicates the position of the Gulf Stream off the east coast of North America as well as the mesoscale eddies associated with it. The geostrophic velocity field is overlaid on the *SSH*. The mesoscale field generates large deviations from the mean. The variations induced by the mesoscale are the driving reason behind many operational systems that require continuous altimeter data input. Courtesy: Charles N. Barron, Naval Research Laboratory.

As discussed in Section 2.3, there is a trade-off between the repeat time of the satellite and the distance between ground tracks. This determines the spatial and temporal resolution of the observation system. The size and time scales of eddies at mid-latitudes are generally not observable by a single altimeter satellite. While the TOPEX temporal sampling may be adequate for most mesoscale features, eddies are usually much smaller than the ground track spacing. The ERS geodetic mission with a 16-km track separation at the equator may be sufficient to observe the spatial scales of most mesoscale features, but the temporal resolution of 168 days is inadequate.

It is not possible to obtain a synoptic picture of the mesoscale field based solely on the data from one satellite altimeter alone. Techniques have been devised to join information from several altimeter satellites in conjunction with dynamical mesoscale properties to provide an improved estimate of the synoptic eddy field. The simpler of these techniques uses optimal interpolation, which employs a prescribed covariance function to interpolate the altimeter *SSH* in space and time. The covariance function prescribes eddy dynamical properties such as expected length and time scales, as well as expected propagation speeds. More advanced techniques use numerical models of ocean dynamics in conjunction with methods to join the model solution with altimeter observations. Robinson et al. (1998) provide an overview of the methods used to assimilate observations into numerical models. The numerical model assimilation methods have shown great promise with significant skill in predicting out to 30 days.

In the deep ocean, mesoscale eddies are ubiquitous features. In a simplified manner, the deep ocean may be viewed as layers of fluids within which different dynamic processes dominate. Near the ocean surface (within about 30 m, though at times much deeper), fluxes of momentum from wind stress and heat are strong contributors to circulation variations. The rate at which surface fluxes mix into the ocean depends primarily on turbulence generated by wind stress, surface waves, and internal waves. Variations occur on relatively short

time periods (on the order of hours to days) in the surface mixed layer. Aside from the mixed layer, the open ocean may be generally viewed as a warm water mass overlying a colder denser water mass. The thermocline is usually the boundary that separates the two water masses. Velocities above the thermocline are much larger than velocities below. This vertical velocity gradient or shear provides the energy to generate the mesoscale variability through the baroclinic instability process (Pedlosky 1979).

The areas in the world in which the strongest vertical shear exists are the western boundary currents such as the Gulf Stream in the Atlantic and the Kuroshio Current in the Pacific. These currents flow northward along the western boundary of the ocean basins, bringing warm water from the tropics to areas far north. The mesoscale eddy field associated with these currents is intense and produces large *SSH* variations (Figure 2-6a). The nonlinear advection of momentum is large in the mesoscale field. The balance of nonlinear advection and the latitudinal variations of the Coriolis parameter creates the tendency for mesoscale features to propagate westward. The difference between the linear and nonlinear mean ocean circulation response to wind stress (Figures 2-2c and 2-2d) indicates substantial shifts in the positions of the Gulf Stream and Kuroshio Current paths. In addition, the mesoscale variability plays a key role in reducing the strength of the Antarctic Circumpolar Current, which is far stronger in the linear global model solution (Figure 2-2c) than observed (Figure 2-2b). This is one example of the turbulent mixing due to the mesoscale field that acts as diffusion on the larger scale circulation.

Observations of the mesoscale field are important not only for research into the fundamental ocean physics but also for deep-ocean monitoring and prediction. Given an accurate model and accurate forcing (wind stress and heat fluxes), the ocean model will generate mesoscale eddies. The model may generate eddies with characteristics (size, propagation speed, decay time, etc.) similar to observed eddies. However, the mesoscale field is nondeterministic. A small perturbation in the model's initial conditions will grow over time. The model will not generate exactly the same eddy that is observed in the ocean at the same time. Continuous observations are required for numerical model assimilation to provide accurate ocean forecasts. Several operational centers exist to provide ocean information (the National Oceanic and Atmospheric Administration, NOAA; the Naval Oceanographic Office, NAVOCEANO; and the group Developing Use of Altimetry for Climate Studies, DUACS). The altimeter satellite provides continuous observations, and these observations are assimilated into numerical models so that the models represent the synoptic mesoscale field.

2.9 MEAN SEA LEVEL AND CLIMATE CHANGE

With the improved measurement accuracy and long time series of TOPEX/Poseidon observations, processes that were previously below the noise floor are now resolvable. The globally averaged sea level change and the spatial variations associated with climate change are important not only for understanding the ocean system but also for future planning. Proper resource management requires knowledge of the effects of changes in ocean circulation, temperatures and nutrients on coastal environments, and subsequent effects on resources such as fish stock.

Because long-term sea level change is expected to be on the order of millimeters per year, careful calibration of the altimeter system must be carried out in order to ensure the accuracy and fidelity of the estimated rise. Two *in situ* calibration sites were originally set up to provide independent sea level height above the reference ellipsoid for direct comparison to TOPEX/Poseidon. These sites are the Harvest oil platform near Catalina Island off the California coast and the site at Lampadusa off the coast of Italy. These sites are surveyed using GPS and are instrumented with accurate tide gauge systems to provide the sea level.

Comparisons to the TOPEX/Poseidon altimeter show less than 5 mm of bias with about 2 mm/year of drift (Christensen et al. 1994; Nerem et al. 1997).

Tide gauge stations have been previously used to examine long time period sea level change. However, there are several drawbacks to using only tide gauges. Tide stations are typically located on coastlines. The local coastal geometry and bathymetry greatly affect not only the regional tides but also long time period change in sea level. The tide gauge spatial distribution is not regular or sufficiently global in nature. Many tide gauges are located along tropical Pacific islands. The long time period ocean circulation changes and associated sea level rise are not expected to simply be an equal increase at every point throughout the world. Circulation changes will vary throughout the globe, and a spatially biased sampling of the sea level will provide a biased view of how the ocean circulation may be changing. Obtaining long records from tide gauges is difficult. A station must be maintained and continually calibrated for accuracy. Movement of the Earth crust changes the position of a tide gauge relative to the geoid. Thus when inferring sea level changes the slow tectonic movement may appear as a sea level change.

The altimeter satellite alleviates several of the difficulties associated with using only tide gauges for estimating climate change. The altimeter satellite spatial distribution of sea level sampling is much more uniform and has much greater coverage than afforded by tide gauges. This reduces problems with observing the spatially varying features associated with climate change. However, accurate calibration of the altimeter instrument using only onboard monitoring equipment is a challenging and difficult task. A small long-period drift in the altimeter instrument or other onboard hardware can appear as a long-period sea level rise. The satellite altimeter and tide gauges provide complementary systems that together are able to overcome the individual difficulties and monitor the long time period changes in ocean circulation. Typically, the global tide gauge sea level variations are used to provide bias and drift estimates for the altimeter satellite. Corrections are made to the satellite data, and then the corrected data are used to examine the long period changes (Mitchum 1998; Nerem et al. 1999).

Two dominant processes change sea level over long time periods. The first process is the change in the liquid/solid ratio of water throughout the world, which is a measure of the mass of ice stored in the polar ice caps. The second process is the thermal expansion or steric anomaly due to warming of the upper ocean. Both these processes may be related to global warming or climate change. If solid ice were to melt to liquid water, or additional heat were added to the oceans, the sea level would be expected to rise. Based on the TOPEX/Poseidon measurements, Nerem et al. (1999) estimated a global sea level rise rate of 2.6 mm/year. An updated analysis including Jason-1 data indicates 2.9 mm/year (Figure 2-7). However, it is difficult to determine if this quantity indicates human-induced or natural changes in the planetary system.

In addition to knowing the rate of sea level rise, it is equally important to determine the spatial structure or ocean circulation variations associated with the sea level rise. In order to determine this, Empirical Orthogonal Function (EOF) techniques have been applied to the altimeter data. The EOF technique constructs a set of spatial fields, each of which has an associated time series (Preisendorfer 1988). Each spatial field (referred to as a mode) indicates how variations throughout the globe are correlated to one another. When each mode is multiplied by its time series and all the modes are summed, the original data set is reconstructed. The mode that reconstructs the largest portion of the original data variability is the most significant. The first two most significant *SSH* modes indicate the spatial structure associated with long period changes (Figure 2-8). In addition to the EOF decomposition of the *SSH*, an EOF decomposition of the sea surface temperature (*SST*) observed by satellite is also constructed. The *SST* and *SSH* variations are well correlated both in the spatial structure and in the temporal variability. This global coverage would not be possible without satellite altimeter instruments.

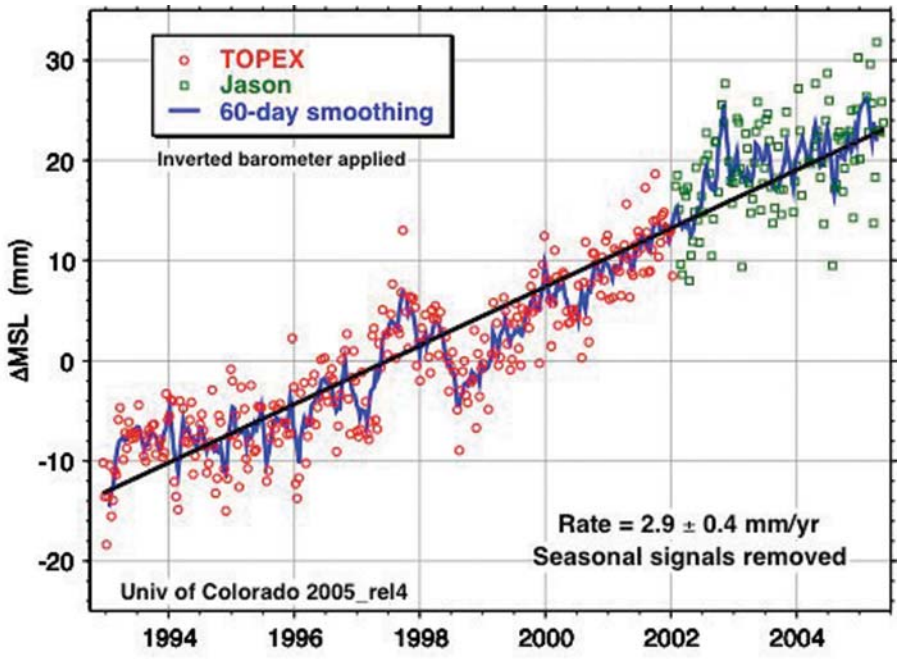

Figure 2-7 The globally averaged sea-surface-height time series based on TOPEX/Poseidon and Jason-1 data indicates the slowly rising sea level. Individual points are 10-day averages, and the solid line is a 60-day filter. Tide gauges provide calibration for the time series, and the altimeter observations provide global coverage to avoid spatial biases. Thus the two systems provide necessary complementary observations. The larger peaks in 1998 and 2002 are results of additional heat content in the equatorial Pacific during El Niño events. Courtesy: Eric Leuliette and R. Steven Nerem.

2.10 CONCLUSIONS

The altimeter satellite hardware, accuracy in corrections, orbit solution methods, and techniques to use the data have all improved over the past decades. The combined research and technology has allowed scientists to understand the altimeter information and its implications on a wide range of ocean large-scale circulation variations. The geophysical applications to which the data are applied have expanded greatly and still continue to expand.

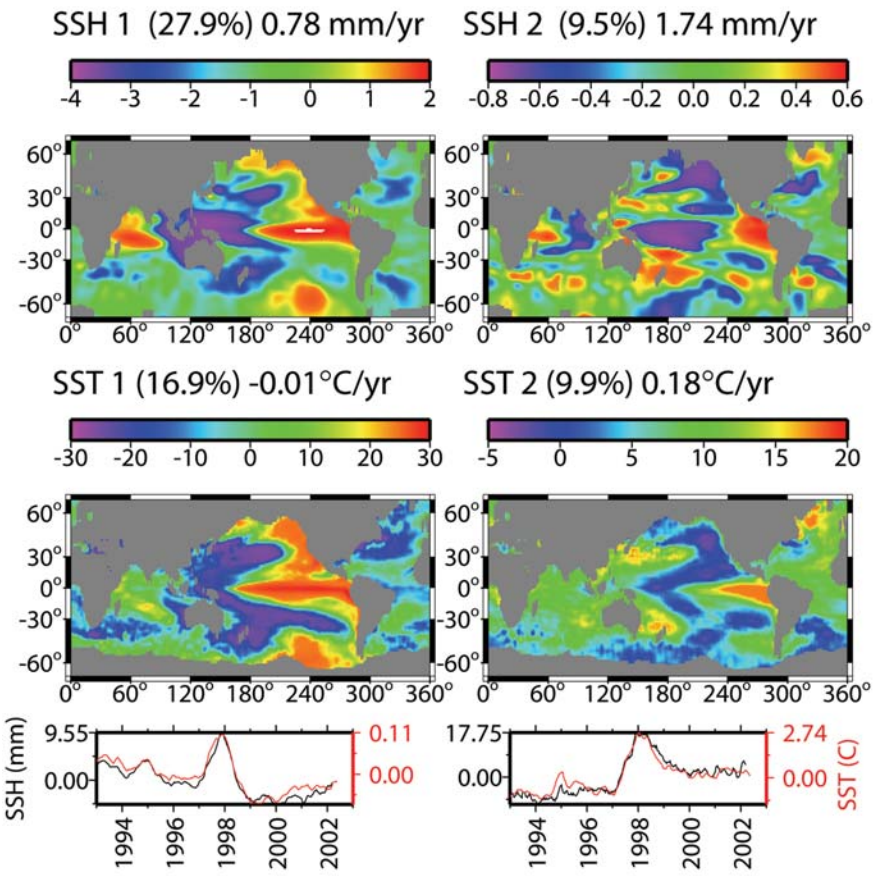

Figure 2-8 The spatial patterns of sea-level height variations provide indicators of environmental change. These changes are a result of many contributors, including ocean circulation, water mass exchange between the ice caps and liquid ocean, and thermal expansion due to heat content changes. For example, the deviations during 1997 are due to the El Niño event that altered the heat content within the tropical Pacific Ocean. This EOF decomposition provides an indication of the spatial structure and temporal variations of the long-period sea level variations. The *SSH* (top) and *SST* (middle) of each of the first two modes (left and right) provide the spatial structure, while the time series (bottom) provides the variations throughout the 10-year time period. Courtesy: R. Steven Nerem.

References

Apel, J. R. 1987. *Principles of Ocean Physics*. New York: Academic Press.

Brenner, A. C., C. J. Koblinsky, and B. D. Beckley. 1990. A preliminary estimate of geoid-induced variations in repeat orbit satellite altimeter observations. *J. Geophys. Res*. 95:3033–3040.

Chelton, D. B., J. C. Ries, B. J. Haines, L. L. Fu, and P. S. Callahan. 2001. Satellite altimetry. In *Satellite Altimetry and Earth Sciences*, edited by L. L. Fu and A. Cazenave. New York: Academic Press.

Christensen, E. J., B. J. Haines, S. J. Keihm, C. S. Morris, R. A. Norman, G. H. Purcell, B. G. Williams, B. D. Wilson, G. H. Born, M. E. Parke, S. K. Gill, C. K. Shum, B. D. Tapley, R. Kolenkiewicz, and R. S. Nerem. 1994. Calibration of TOPEX/Poseidon at Platform Harvest. *J. Geophys. Res.* 99, C12:24465–24485.

Csanady, G. T. 1984. *Circulation in the Coastal Ocean*. Boston: D. Reidel Publishing Co.

Doodson, A. T. and H. D. Warburg. 1941. *Admiralty Manual of Tides*. London: Her Majesty's Stationery Office.

Freedman, A. P. and B. Parsons. 1986. Seasat-derived gravity over the Musician seamounts. *J. Geophys. Res*. 91:8325–8340.

Fu, L. L. and R. Cheney. 1995. Application of satellite altimetry to ocean circulation studies: 1987–1994. *Rev. Geophys*. 33 Suppl.:213–223.

Fu, L. L., E. J. Christensen, C. A. Yamerone Jr, M. Lefebvre, Y. Ménard, M. Dorrer, and P. Escudier. 1994. TOPEX/POSEIDON mission overview. *J. Geophys. Res.* 99:24369–24381.

Hsueh, Y. 1988. Recent current observations in the eastern Yellow Sea. *J. Geophys. Res.* 93:6875–6884.

Jacobs, G. A. 1998. Sea surface height variations in the Yellow and East China Seas, 1. Linear response to local wind stress, *J. Geophys. Res.*, 103, 18,459-18,477.

Jayne, S. R. and S. Marotzke. 2002. The ocean eddy heat transport. *J. Phys. Oceanogr*. 32:3328–3345.

Le Provost, C., F. Lyard, J. M. Molines, M. L. Genco, and F. Rabilloud. 1998. A hydrodynamic ocean tide model improved by assimilating a satellite altimeter-derived data set. *J. Geophys. Res.* 103:5513–5529.

Marsh, J. G. and T. V. Martin. 1982. The Seasat altimeter mean sea surface model. *J. Geophys. Res.* 87:3269–3280.

Mitchum, G. T. 1998. Monitoring the stability of satellite altimeters with tide gauges. *J. Atmos. and Oceanic Tech.* 15:721–730.

Nerem, R. S., B. J. Haines, J. Hendricks, J. F. Minster, G. T. Mitchum, and W. B. White. 1997. Improved determination of global mean sea level variations using TOPEX/Poseidon altimeter data. *Geophys. Res. Let.* 1331–1334.

Nerem, R. S., D. P. Chambers, E. W. Leuliette, G. T. Mitchum, and B. S. Giesse. 1999. Variations in global mean sea level associated with the 1997–1998 ENSO event: Implications for measuring long term sea level change. *Geophys. Res. Let.* 26:3005–3008.

Pedlosky, J. 1987. *Geophysical Fluid Dynamics.* 2nd ed. New York: Springer Verlag.

Pickard, G. L. and W. J. Emery. 1982. *Descriptive Physical Oceanography*. Elmsford, N.Y.: Pergamon Press.

Preisendorfer, R. W. 1988. *Principal Component Analysis in Meteorology and Oceanography*. New York: Elsevier.

Robinson, A. R., P.F.J. Lermusiaux, and N. Q. Sloan III. 1998. Data assimilation. In *The Sea*, Vol. 10, edited by K. H. Brink and A. R. Robinson. New York: Wiley.

Sandwell, D. T. 1991. Geophysical applications of satellite altimetry. *Rev. Geophys. Suppl.* 29:132–137.

Sandwell, W. T. and W.H.F. Smith. 1997. Marine gravity anomaly from Geosat and ERS-1 satellite altimetry. *J. Geophys. Res.* 102:10039–10054.

Schlax, M. G. and D. B. Chelton. 1994. Aliased tidal errors in TOPEX/Poseidon sea-surface height data. *J. Geophys. Res.* 99, C12:24761–24775.

Schouten, M. W., P. M. Will de Ruijter, P. J. van Leeuwen, and J.R.E. Lutjeharms. 2000. Translation, decay and splitting of Agulhas rings in the southeastern Atlantic Ocean. *J. Geophys. Res.* 105, no. 21:913–921, 925.

Schwiderski, E. W. 1980. Ocean tides, II, A hydrodynamic interpolation model. *Marine Geodesy* 3:219–255.

Shum, C. K., P. L. Woodworth, O. B. Andersen, G. D. Egbert, O. Francis, C. King, S. M. Klosko, C. Le Provost, X. Li, J. M. Molines, M. E. Parke, R. D. Ray, M. G. Schlax, D. Stammer, C. C. Tierney, P. Vincent, and C. I. Wunsch. 1997. Accuracy assessment of recent ocean tide models. *J. Geophys. Res.* 102:25173–25194.

Smith, W.H.F. 1998. Seafloor tectonic fabric from satellite altimetry. *Ann. Rev. Earth and Plan. Studies* 26:697–747.